APPLIED SCIENCES AND ENGINEERING

Broadband sensory networks with locally stored responsivities for neuromorphic machine vision

Guo-Xin Zhang[1]†, Zhi-Cheng Zhang[2]†, Xu-Dong Chen[1,2]*, Lixing Kang[3], Yuan Li[2], Fu-Dong Wang[1], Lei Shi[1], Ke Shi[1], Zhi-Bo Liu[2], Jian-Guo Tian[2], Tong-Bu Lu[1]*, Jin Zhang[4]*

As the most promising candidates for the implementation of in-sensor computing, retinomorphic vision sensors can constitute built-in neural networks and directly implement multiply-and-accumulation operations using responsivities as the weights. However, existing retinomorphic vision sensors mainly use a sustained gate bias to maintain the responsivity due to its volatile nature. Here, we propose an ion-induced localized-field strategy to develop retinomorphic vision sensors with nonvolatile tunable responsivity in both positive and negative regimes and construct a broadband and reconfigurable sensory network with locally stored weights to implement in-sensor convolutional processing in spectral range of 400 to 1800 nanometers. In addition to in-sensor computing, this retinomorphic device can implement in-memory computing benefiting from the nonvolatile tunable conductance, and a complete neuromorphic visual system involving front-end in-sensor computing and back-end in-memory computing architectures has been constructed, executing supervised and unsupervised learning tasks as demonstrations. This work paves the way for the development of high-speed and low-power neuromorphic machine vision for time-critical and data-intensive applications.

INTRODUCTION

Machine vision plays a crucial role in time-critical applications, which require real-time object recognition and classification, such as autonomous driving and robotics (*1*). With the increase of frame rates and pixel densities of sensors, large quantities of raw and unstructured data are generated in sensory terminals (*2*, *3*), and image processing becomes a data-intensive task, which requires high-efficiency and low-power image processing directly at the sensory terminals (*2*, *4*, *5*). The emerging in-sensor computing that can perform low-level and high-level image processing tasks in sensory networks has attracted numerous attentions in recent years, and various neuromorphic devices and structures including optoelectronic synapses (*6*–*11*) and one-photosensor–one-memristor arrays (*3*, *12*) have been developed to implement in-sensor computing. In particular, human retina–inspired retinomorphic vision sensors have demonstrated their great potential in in-sensor computing because they can constitute built-in artificial neural networks (ANNs) and implement multiply-and-accumulation (MAC) operations using tunable responsivities as the weights of ANNs (*1*, *13*–*18*). However, these retinomorphic devices still suffer from the volatile nature of their responsivities, which require a sustained gate bias to maintain (*1*, *13*, *14*, *19*, *20*). That is, the weights of ANNs need to be stored remotely and supplied to each vision sensor via complex external circuits, which would inevitably consume additional energies. More seriously, extremely complex circuits are required for the individual control of each unit in networks, which is almost impossible and unacceptable for large-scale sensory networks considering the limited power and resources available at the edge. In addition, the limited operating spectra of these retinomorphic devices, mainly in ultraviolet (UV) and visible (vis) range (*1*, *13*, *15*, *16*, *19*, *20*), hinder the implementation of in-sensor computing in more important infrared band. It is highly desirable to develop broadband retinomorphic vision sensors with nonvolatile tunable responsivities to constitute sensory networks for neuromorphic machine vision.

Here, we propose an ion-induced localized-field modulation strategy to realize the nonvolatile modulation of responsivity and develop a broadband retinomorphic vision sensor with operating spectra covering 400 to 1800 nm based on core-sheath single-walled carbon nanotube@graphdiyne (SWNT@GDY). The responsivity can be linearly modulated in both positive and negative regimes by controlling the localized field induced by the trapped Li^+ ions in GDY, enabling the implementation of in-sensor MAC operation and convolutional processing. A $3 \times 3 \times 3$ sensor array is fabricated to constitute a reconfigurable convolutional neural network (CNN) involving three kernels (3×3), and low-level and high-level processing tasks for multiband images, including edge detection and sharpness of hyperspectral images and classification of colored letters, are performed as demonstrations. The conductance of this retinomorphic device can also be linearly modulated, and, thus, the device array can also implement in-memory computing tasks. A complete hardware emulation of human visual system including retina and brain visual cortex is achieved by networking the front-end in-sensor CNN and back-end in-memory ANN based on the same device structure, and unsupervised learning (autoencoder) is demonstrated. The nonvolatile nature of responsivity induced by the localized field enables the local storage of weights

[1]MOE International Joint Laboratory of Materials Microstructure, Institute for New Energy Materials and Low Carbon Technologies, School of Material Science and Engineering, Tianjin University of Technology, Tianjin 300384, China. [2]The Key Laboratory of Weak Light Nonlinear Photonics, Ministry of Education, School of Physics, Nankai University, Tianjin 300071, China. [3]Key Laboratory of Multifunctional Nanomaterials and Smart Systems Division of Advanced Material, Suzhou Institute of Nano-Tech and Nano-Bionics, Chinese Academy of Sciences, Suzhou 215123, China. [4]Center for Nanochemistry, Beijing Science and Engineering Center for Nanocarbons, Beijing National Laboratory for Molecular Sciences, College of Chemistry and Molecular Engineering, Peking University, Beijing 100871, China.
*Corresponding author. Email: chenxd@nankai.edu.cn (X.-D.C.); lutongbu@tjut.edu.cn (T.-B.L.); jinzhang@pku.edu.cn (J.Z.)
†These authors contributed equally to this work.

in sensory networks, which is essential for high-efficiency low-power in-sensor computing at edge.

RESULTS

Broadband retinomorphic vision sensor with nonvolatile responsivity

Figure 1A illustrates the schematic of human visual system, in which visual information is sensed and preprocessed in retina, and the extracted features (encoded data) are then transmitted to visual cortex in the brain for further processing (21, 22). The front-end retina plays a crucial role in this system because it can greatly reduce the delivered data to the brain by executing first-stage processing. Inspired by human visual system, neuromorphic machine vision composed of front-end in-sensor computing and back-end in-memory

computing architectures (Fig. 1B) provides a high-efficiency and low-power solution for real-time and data-intensive tasks by processing the captured images directly at the sensory terminals. Compared to the well-studied and gradually mature in-memory computing architecture (23–26), the crucial in-sensor computing, however, still requires more efforts.

To emulate the functions of human retina and implement in-sensor computing, retinomorphic vision sensors based on core-sheath SWNT@GDY nanotubes were fabricated by Aerosol Jet printing (Fig. 1, C and D; details in Materials and Methods and figs. S2 and S3). The core-sheath SWNT@GDY nanotubes, which were synthesized via a solution-phase epitaxial strategy (note S1) (27–31), were well designed to realize the nonvolatile modulation of responsivity in both positive and negative regimes. As described in note S2 and figs. S4 to S10, GDY is crucial for the intercalation of
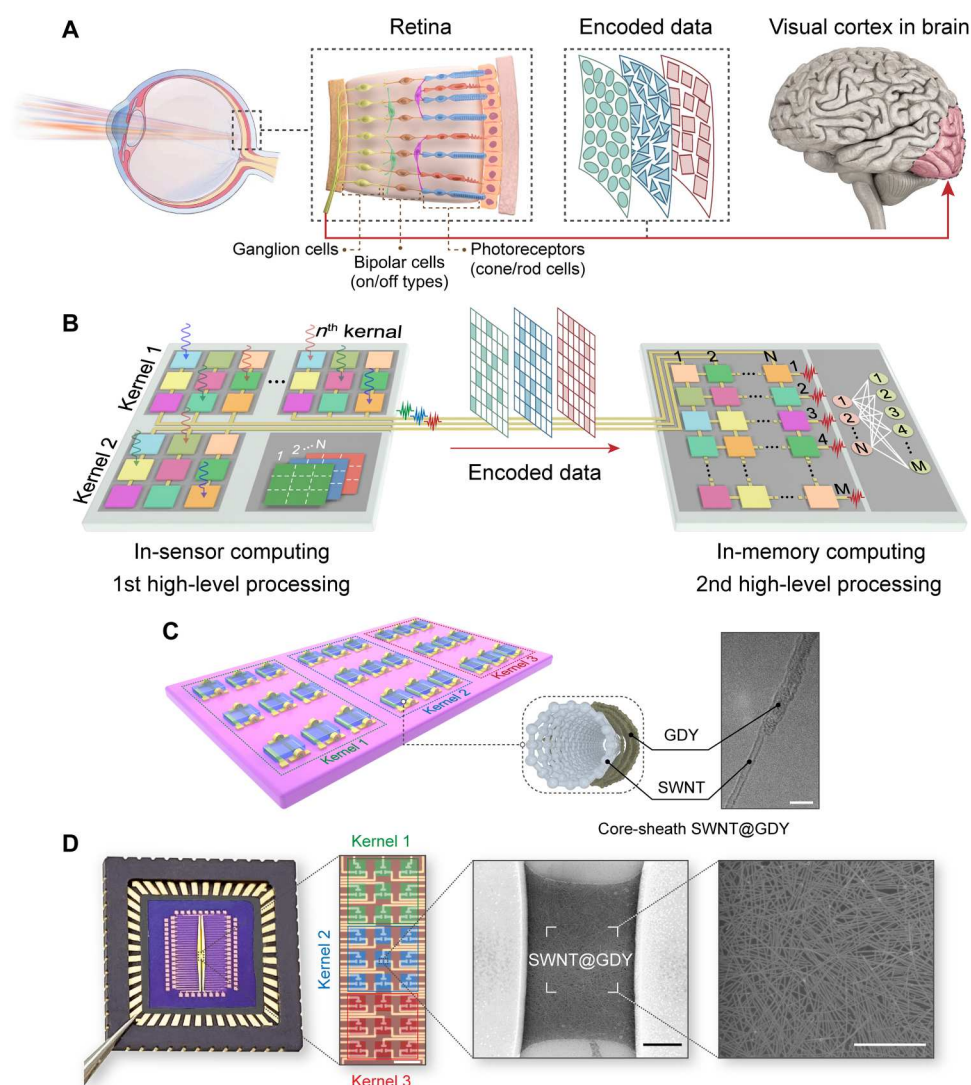

Fig. 1. Neuromorphic visual systems inspired by human visual system. (**A**) Schematic of human visual system consisting retina and brain visual cortex. (**B**) A complete neuromorphic visual system involving front-end in-sensor computing and back-end in-memory computing. (**C**) Schematic of sensory networks based on core-sheath SWNT@GDY nanotubes. The middle and right panels show the structure and high-resolution transmission electron microscopy image of the core-sheath SWNT@GDY nanotube. Scale bar, 5 nm. (**D**) Photograph, optical microscopy, and scanning electron microscopy images of a $3 \times 3 \times 3$ sensor array divided into three kernels. Scale bars (left to right), 50, 2, and 1 μm, respectively.

Li$^+$ ions and the nonvolatile modulation of conductance and responsivity, benefiting from its evenly distributed large pores and high Li$^+$-ion storage capability (*32*, *33*). Li$^+$ ions in electrolyte can penetrate into GDY layer driven by a small gate bias and store in GDY even after removing the external gate bias (fig. S4). The thickness of the sheath GDY layer was approximately 1 nm, as a thicker GDY layer would obstruct the light absorption of core SWNT and restrict the charge transport between the electrodes and SWNT channel (note S2).

Figure 2A shows the collective transfer curves of the device with gate voltage (V_G) sweeping from −0.5 to 0.5 V and back to −0.5 V. A clockwise hysteresis with an on/off ratio of over 10^3 at $V_G = 0$ V is observed, which is induced by the intercalation of Li$^+$ ions in GDY (*32*). The reduced conductance after sweeping is ascribed to the residual Li$^+$ ions trapped in GDY, and it can return to its initial state

while prolonging the time for Li$^+$-ion extraction (fig. S12). The density of Li$^+$ ions in GDY can be precisely controlled by applying positive or negative V_G pulses. As shown in Fig. 2B and fig. S13, the conductance was linearly modulated from 7.0 to 0.3 nS with 64 discrete states by applying V_G pulses (0.5 V, 1 ms). These conductance states exhibit nonvolatile characteristics with retention time of over 10^4 s (fig. S14), which indicates the stability of the intercalated Li$^+$ ions in GDY. A reversible and repeatable conductance update with high linearity and symmetricity was achieved as shown in Fig. 2C, demonstrating its potential in neuromorphic computing (*34*, *35*). The energy consumption for each update operation is calculated as low as 50 aJ ($E = V_G \times I_{GS} \times t_{duration}$), considering the leakage current I_{GS} in order of 10^{-13} A (fig. S15). The cyclic endurance of the device was measured by alternatively applying positive and negative V_G pulses for 10^5 cycles (fig. S16), and no degradation was
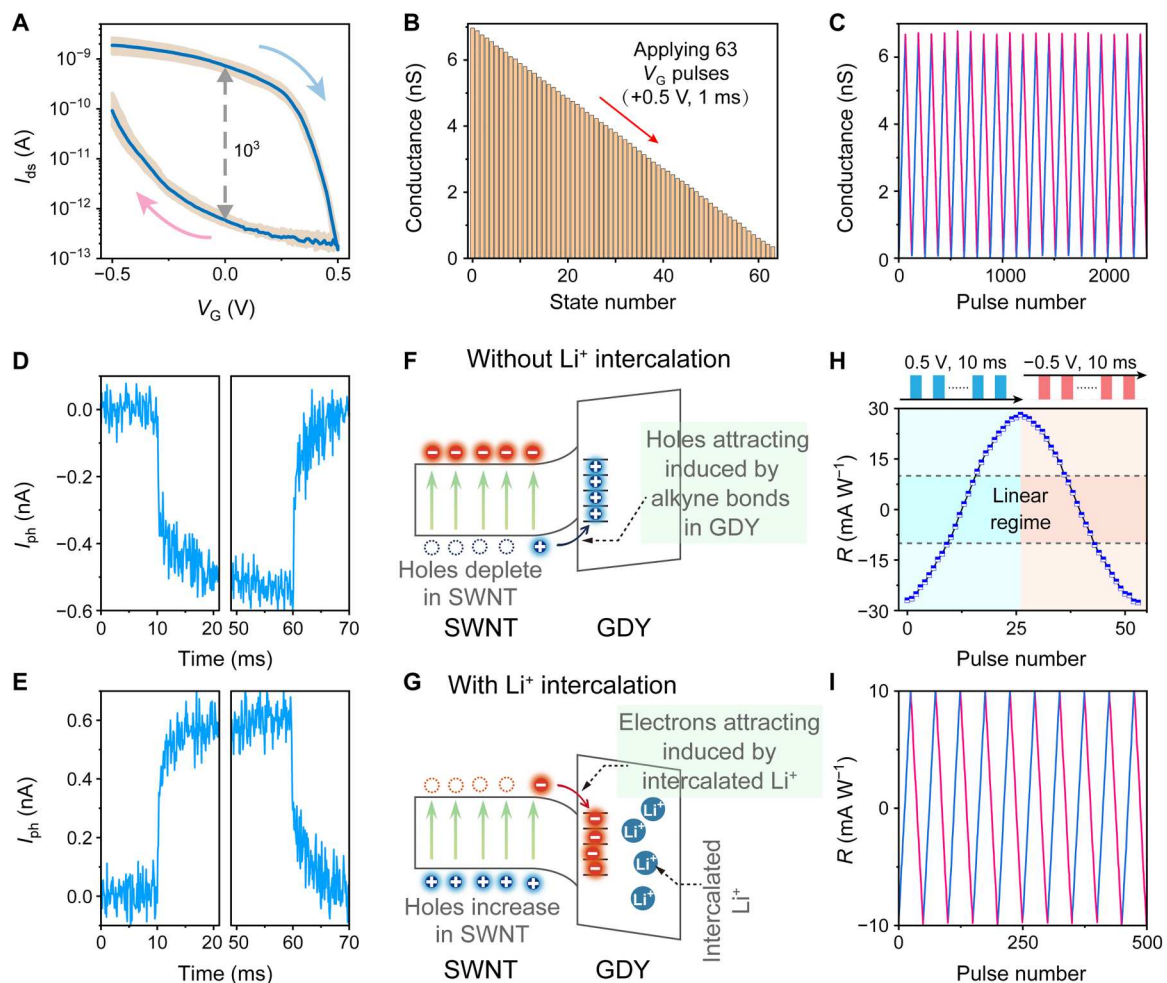

Fig. 2. Retinomorphic vision sensors with nonvolatile conductance and responsivity. (**A**) Transfer curves with V_G sweeping from −0.5 to 0.5 V and back to −0.5 V. (**B**) Sixty-four discrete conductance states realized by applying 0.5-V, 1-ms V_G pulses. (**C**) Linear, symmetric, and repeatable conductance-update curves obtained by alternatively applying 64 positive and 64 negative V_G pulses (±0.5 V, 1 ms). (**D** and **E**) Negative (D) and positive (E) photoresponse triggered by a 532-nm optical pulse. A 0.1-V read voltage (V_{ds}) was used. (**F** and **G**) Band alignments and charge transfer for the SWNT/GDY heterostructure without (F) and with (G) Li$^+$-ion intercalation in GDY layer. Without Li$^+$ intercalation, the hole-attracting alkyne bonds in GDY induce the transfer of photogenerated holes from SWNT to the charge trapping sites in GDY, resulting in the decrease of the hole concentration (majority carrier) in SWNT and thus a negative photocurrent. With numerous Li$^+$ intercalation, positively charged Li$^+$ ions attract photogenerated electrons transfer from SWNT to GDY, inducing the increase of hole concentration in SWNT and thus a positive photocurrent. (**H**) Symmetric and reversible modulation of the responsivity in positive and negative regimes by applying positive and negative V_G pulses (±0.5 V, 10 ms). (**I**) Linear, reversible, and repeatable modulation of responsivity in range of ±10 mA W^{-1} by controlling the density of intercalated Li$^+$ ions in GDY.

observed for both the high- and low-conductance states during the whole test. All these results demonstrate that frequent and repetitive intercalation/extraction of Li$^+$ ions would not destroy the structure and degrade the performance of our device.

The intercalated Li$^+$ ions in GDY also induce a notable modulation of the device photoresponse. As shown in Fig. 2 (D and E), a negative photoresponse was observed for the device without Li$^+$-ion intercalation, while a positive photoresponse with comparable amplitude can be achieved by intercalating Li$^+$ ions into GDY. This can be explained by the transition of GDY from hole-attracting to electron-attracting with the intercalation of Li$^+$ ions. GDY contains numerous alkyne bonds that are quite active as positive-charge–attracting magnets (36, 37). For the case without Li$^+$-ion intercalation, these positive-charge–attracting magnets facilitate the separation and transfer of photogenerated holes from SWNT to GDY (Fig. 2F), leading to a negative photoresponse considering the p-type nature of SWNT. With the intercalation of Li$^+$ ions, a localized electrostatic field is formed from GDY to SWNT, preventing the injection of holes and offsetting the hole-attracting of alkyne bonds. While the electrostatic field is strong enough, the GDY layer will attract photogenerated electrons and thus induce a positive photoresponse (Fig. 2G). The competition between the hole-attracting of alkyne bonds and electron-attracting of Li$^+$ ions in GDY makes it possible to modulate the photoresponse continuously in negative and positive regimes. As shown in Fig. 2H and fig. S17, by controlling the density of intercalated Li$^+$ ions in GDY, a symmetrical, reversible, and nonvolatile modulation of responsivity was achieved, which was almost linear in range of ±10 mA W^{-1} (Fig. 2I). The core-sheath structure and π-conjugated coupling of the two carbon allotropes, SWNT and GDY, enable the fast transfer of carriers between SWNT and GDY, and the timescale of the photoresponse is in several milliseconds (Fig. 2, D and E). The response speed is mainly limited by the charge trapping/detrapping mechanism of the device. In addition, given the parasitic capacitance for micro/nano devices usually in orders of femtofarad to sub-picofarad and the high resistance of the device (10^8 to 10^9 ohms), the resistance-capacitance (RC) time constant is in orders of microsecond to sub-millisecond, which is another important factor that limits the further improvement of response speed.

Linear and identical weight update for sensory network

A 3 × 3 × 3 retinomorphic sensor array (Fig. 1D) was fabricated to implement in-sensor computing. For neuromorphic hardware systems, the performance identity and reliability of each element in the neural network are essential for high computing accuracy. To minimize the influence of device-to-device variation and cycle-to-cycle variation for weight update, here, we used a closed-loop programming operation (25) to program the conductance states and responsivities of all the 27 vision sensors in the sensory network (note S3 and figs. S18 to S20). As detailedly described in note S3, the conductance and responsivity were equally divided into 32 levels (5 bits) in their linear regions, and all the 27 devices could be programmed to these states precisely and repeatedly (figs. S21 and S22). Figure 3 (A and C) depicts the cumulative probability distribution of the 27 devices with respect to 32 discrete conductance and responsivity states for 1000 repetitions, where all these states are separated without any overlap (figs. S23 and S24). Figure 3B shows the *I-V* curves of the device measured at the 32 conductance states, with an excellent linearity in ±0.2 V regime.

As well, the light intensity–dependent photocurrents were measured (fig. S25), demonstrating a linear relationship for all the 32 responsivities (Fig. 3D). The linear bias-voltage and light-intensity dependence on the drain current and photocurrent enable accurate analog multiplication operations for in-memory and in-sensor computing, respectively.

The broadband absorption of SWNT@GDY (fig. S11) enables the retinomorphic vision sensors to operate in a wide spectral range. The photoresponse of the device triggered by light with wavelengths of 400 to 1800 nm was investigated (fig. S26). The update of responsivities at these wavelengths were also performed using the closed-loop programming method. As shown in Fig. 3E, linear and reversible responsivity updates with 32 discrete levels were achieved for all the six wavelengths, and fig. S27 presents the distribution of the 32 responsivities for all the 27 devices. The linear relationship between light intensity and photoresponse was also demonstrated for the six wavelengths (fig. S28). All these results demonstrate the capability of our retinomorphic vision sensors to implement in-sensor computing for multiband images.

In-sensor convolutional processing of multiband images

The linear modulation of responsivity and linear light-intensity dependence of photocurrent as demonstrated above make it possible to construct a reconfigurable retinomorphic sensory network by connecting the retinomorphic vision sensors in parallel. In-sensor MAC operation, a fundamental operation for in-sensor computing, can be realized by performing a real-time multiplication of optically projected images with responsivity matrix of the sensor array and summing the photocurrents generated by all the vision sensors via Kirchhoff's law. To demonstrate the accuracy of the MAC implemented in our SWNT@GDY-based sensor array, a simple network containing two sensors was first investigated (Fig. 4A). As shown in Fig. 4B, two responsivities, R_1 and R_2, were set to the same and opposite values, respectively, and a sequence of optical pulses with different intensities was projected to the sensors. The measured total photocurrents generated by the two sensors follow the equation of $I_{ph} = R_1 P_1 + R_2 P_2$, confirming the validity of MAC.

The broadband characteristics of the SWNT@GDY-based vision sensors enable the sensing and processing of multiband images, for example, hyperspectral images captured by aircrafts or satellites. Here, a 3 × 3 sensor array with reconfigurable responsivities was used as a convolutional kernel to sense and process hyperspectral images from Urban datasets (Fig. 4C). The detailed process for the convolutional processing is described in Materials and Methods and fig. S29. Three images (100 × 100 pixels) were extracted from the hyperspectral images to represent images in UV, vis, and near-infrared (NIR) bands, respectively. By setting the kernel with different responsivity distributions, the sensing and processing, e.g., edge detection and sharpness, of multiband images were implemented successfully. Figure 4D presents the reconstructed images obtained by sliding the corresponding kernels on multiband images. End-members including "roof," "grass," "tree," and "road" embedded in the multiband images with different wavelengths (fig. S30) were highlighted by the convolutional processing operated in corresponding bands. The good agreement of the experimental results with simulations (fig. S31) verifies the reliability of in-sensor convolutional processing for multiband images in UV-vis-NIR bands.
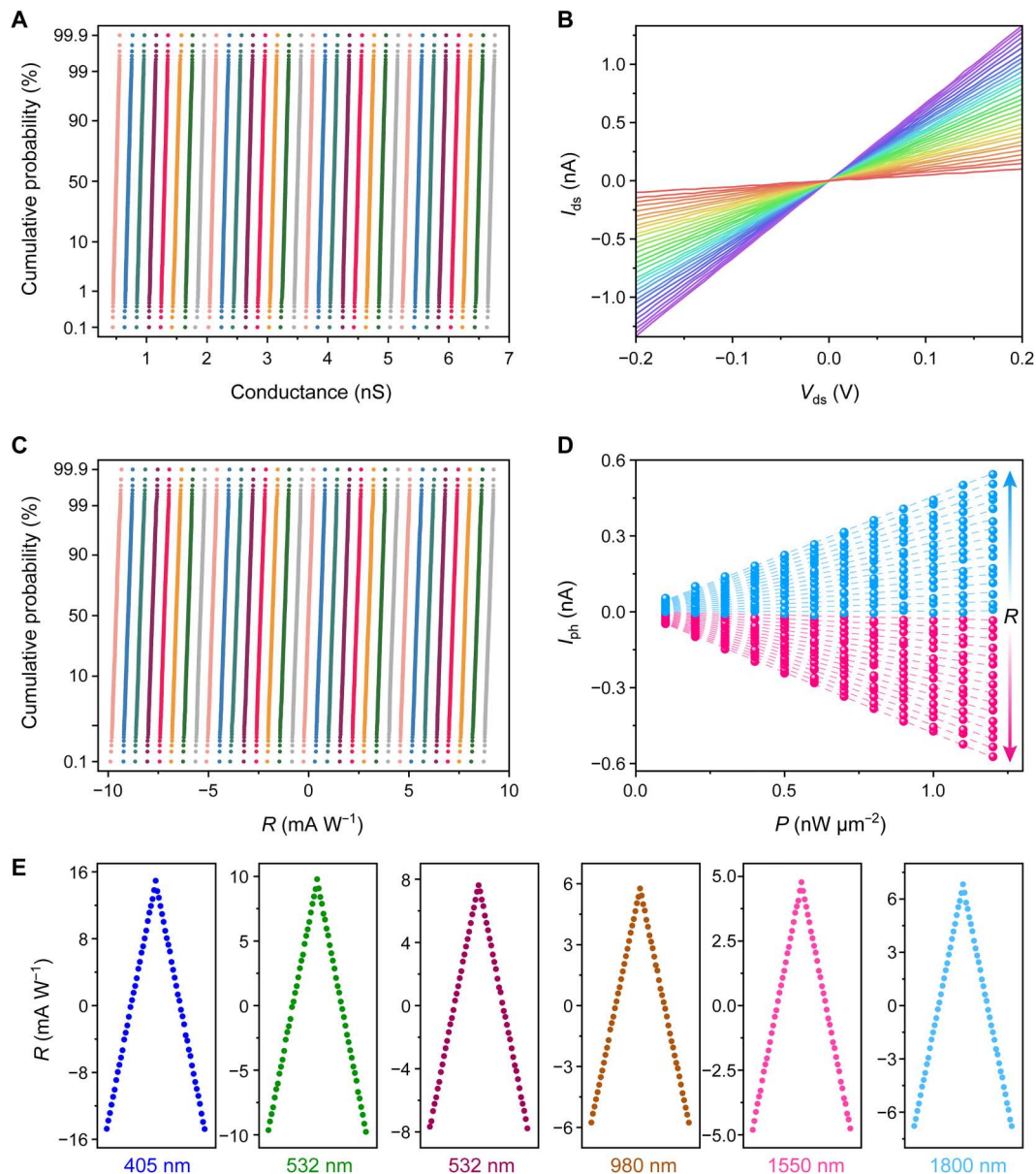
Fig. 3. Linear and identical conductive and photoresponse characteristics for the sensory network. (**A**) Cumulative probability distribution of the whole 27 devices with respect to 32 discrete conductance states for 1000 repetitions. (**B**) I-V curves of the device at the 32 conductance states with V_{ds} sweeping from −0.2 to 0.2 V. (**C**) Cumulative probability distribution of the whole 27 devices with respect to 32 discrete responsivity states for 1000 repetitions. (**D**) Light-intensity dependence of the photocurrents for the device with 32 different responsivities, under irradiation of 532 nm and read voltage of 0.1 V. (**E**) Linear and reversible responsivity updates with 32 discrete states for wavelengths of 405, 532, 633, 980, 1550, and 1800 nm, respectively. The conductance and responsivity in this figure were updated using the close-loop programming method.

In-sensor CNN for classification and autoencoding

The successful implementation of MAC operation demonstrates the potential of this retinomorphic sensor array to constitute a built-in neural network and perform high-level processing tasks, analogous to the function of human retina. On the basis of the fabricated 3 × 3 × 3 sensor array, a CNN containing three convolutional kernels (3 × 3) was constructed to perform color-image classification tasks (Fig. 5A). Three letters of "n," "k," and "u" (3 × 3 pixels) with mixed colors and Gaussian noises (σ = 0, 0.1, 0.2, and 0.3, respectively) were randomly generated as training and test datasets

(Fig. 5B and figs. S32 and S33). In each training epoch, a set of 20 randomly chosen letters was optically projected to three kernels (fig. S34), and the corresponding output photocurrents of each kernel I_m (m = 1, 2, and 3 representing the kernel index) were further non-linearly activated by the Softmax function. The outputs f_1, f_2, and f_3 after activation represent the probabilities for letters n, k, and u, respectively. The weights (responsivities) of each kernel were updated by backpropagating the gradients of loss function (here, cross-entropy function). Figure 5C and fig. S35 present the weight distribution of the three kernels before and after 30 epochs, and fig.
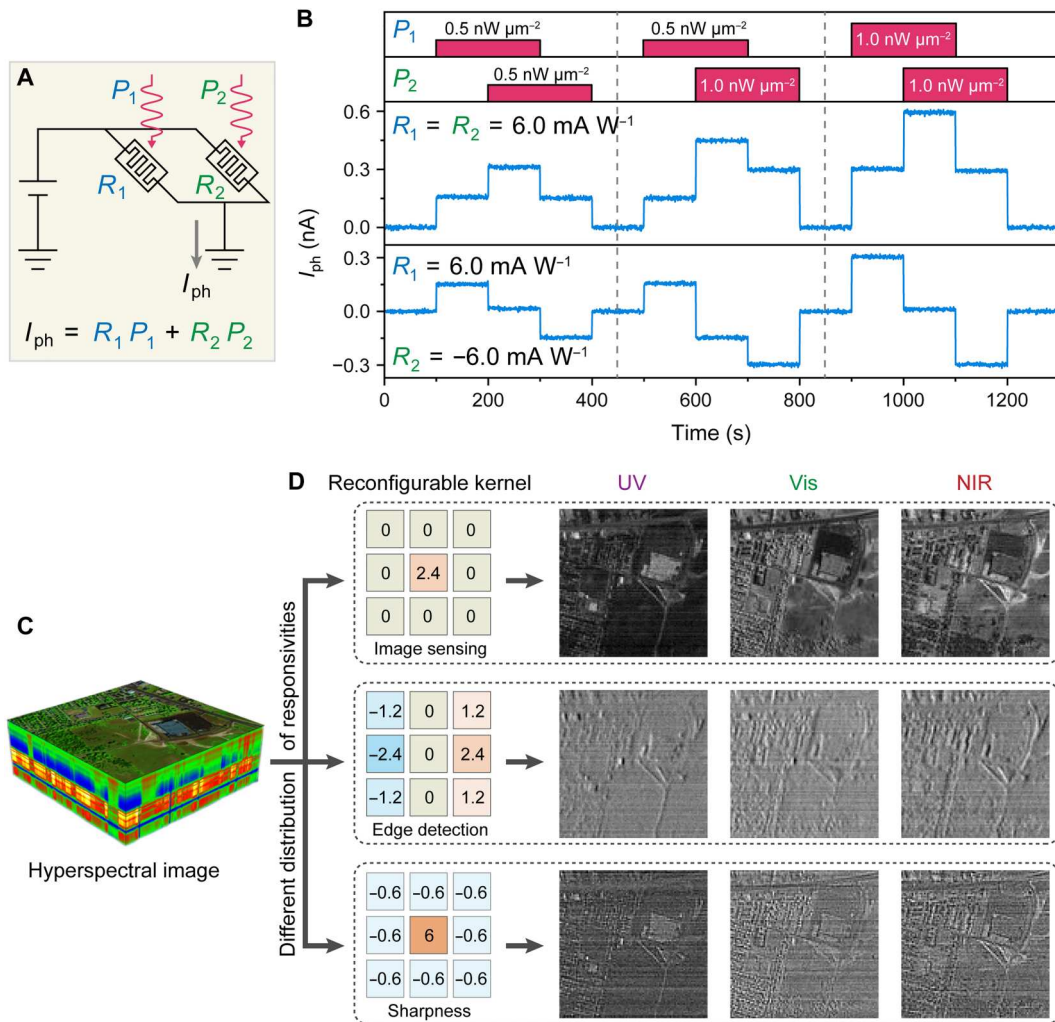
Fig. 4. In-sensor MAC operation and convolutional processing for multiband images. (**A**) Schematic circuit diagram of a sensory network containing two retinomorphic vision sensors for implementation of in-sensor MAC operation. R_1 and R_2 represent the responsivities of the two sensors, while P_1 and P_2 are the corresponding light intensities. (**B**) The output total photocurrent generated by the two sensors by applying irradiation with different intensities. Top: The responsivities of the two sensors were both set as 6.0 mA W^{-1}. Bottom: The responsivities were set as 6.0 and −6.0 mA W^{-1}, respectively. (**C**) Hyperspectral image of Urban (https://rslab.ut.ac.ir/data) (*40*). (**D**) Demonstration of different convolutional processing operations (image sensing, edge detection, and sharpness) in UV, vis, and NIR bands by setting different responsivity distributions of the 3 × 3 kernel.

S36 depicts the evolution of the loss during training. The accuracy of the network was estimated by classifying 100 letters chosen from the test datasets. Although the wavelength-dependent photoresponse would induce slightly degradation in recognition efficiency for mixed-color images (fig. S37), the recognition accuracy still quickly reaches 100% within 10 epochs for σ = 0 and 0.1, and approximately 20 epochs are required for color images with larger noises of σ = 0.2 and 0.3 (Fig. 5D). Figure 5E depicts the evolution of outputs f_1, f_2, and f_3 for letters of n, k, and u with σ = 0.2, and the target image is well separated from the other two letters after 10 epochs, demonstrating the successful classification of color images. Although the wide operation spectral range of the vision sensor enables the recognition of color images, it can just recognize what the letter is (n, k, or u) but still lack the ability to distinguish the color of each pixel. As we emphasized above, the key feature of this retinomorphic vision sensor is the nonvolatile responsivity,

and, thus, the weights can be locally stored in the CNN without external field. Figure S38 presents the evolution of the weights after the last training, and the degradation of the responsivity for each device was approximately 5% in 10 hours. This level of degradation would not influence the classification accuracy of the classifier, which still kept 100% even after 10 hours (fig. S39).

In addition to in-sensor computing, the linear and nonvolatile modulation of the conductance states enables the implementation of in-memory computing. A complete neuromorphic visual system involving front-end in-sensor computing and back-end in-memory computing, analogous to human visual system including retina and visual cortex, was constructed by networking a 3 × 3 × 3 in-sensor CNN with a 3 × 9 in-memory ANN. As a demonstration, unsupervised autoencoding tasks were implemented using the sensory network and ANN to act as encoder and decoder, respectively (Fig. 5F). Grayscale images (3 × 3 pixels) with Gaussian noises

Fig. 5. Implementation of in-sensor CNN for classification and autoencoding. (**A**) Schematic of an in-sensor classifier containing three 3 × 3 kernels for color-image classification. (**B**) Color images of letters n, k, and u with randomly generated colors and Gaussian noises (σ = 0, 0.1, 0.2, and 0.3, respectively). (**C**) Responsivity distributions of the classifier before (initial) and after (final) training for σ = 0.2. (**D**) Classification accuracy of the classifier during training for datasets with different noise levels. (**E**) Average output signals (f_1, f_2, and f_3) for each projected letter, measured during each training epoch with a noise level of σ = 0.2. (**F**) Schematic of an autoencoder using a 3 × 3 × 3 sensory network (in-sensor computing) and a 3 × 9 ANN (in-memory computing) as the encoder and decoder, respectively. (**G**) Autoencoding process using grayscale images with noise level of σ = 0.2 as demonstration. Each input image was translated into a current code with three elements, which were further nonlinearly activated to a set of encoded data approximately in binary and finally reconstructed to a 3 × 3 image by the decoder. (**H**) Reconstructed images of the pretrained autoencoder with locally stored weights (responsivity for encoder and conductance for decoder) for input images with noise levels of σ = 0.2 and 0.3. t represents the time after the last weight update, and autoencoding tasks were implemented with different t values.
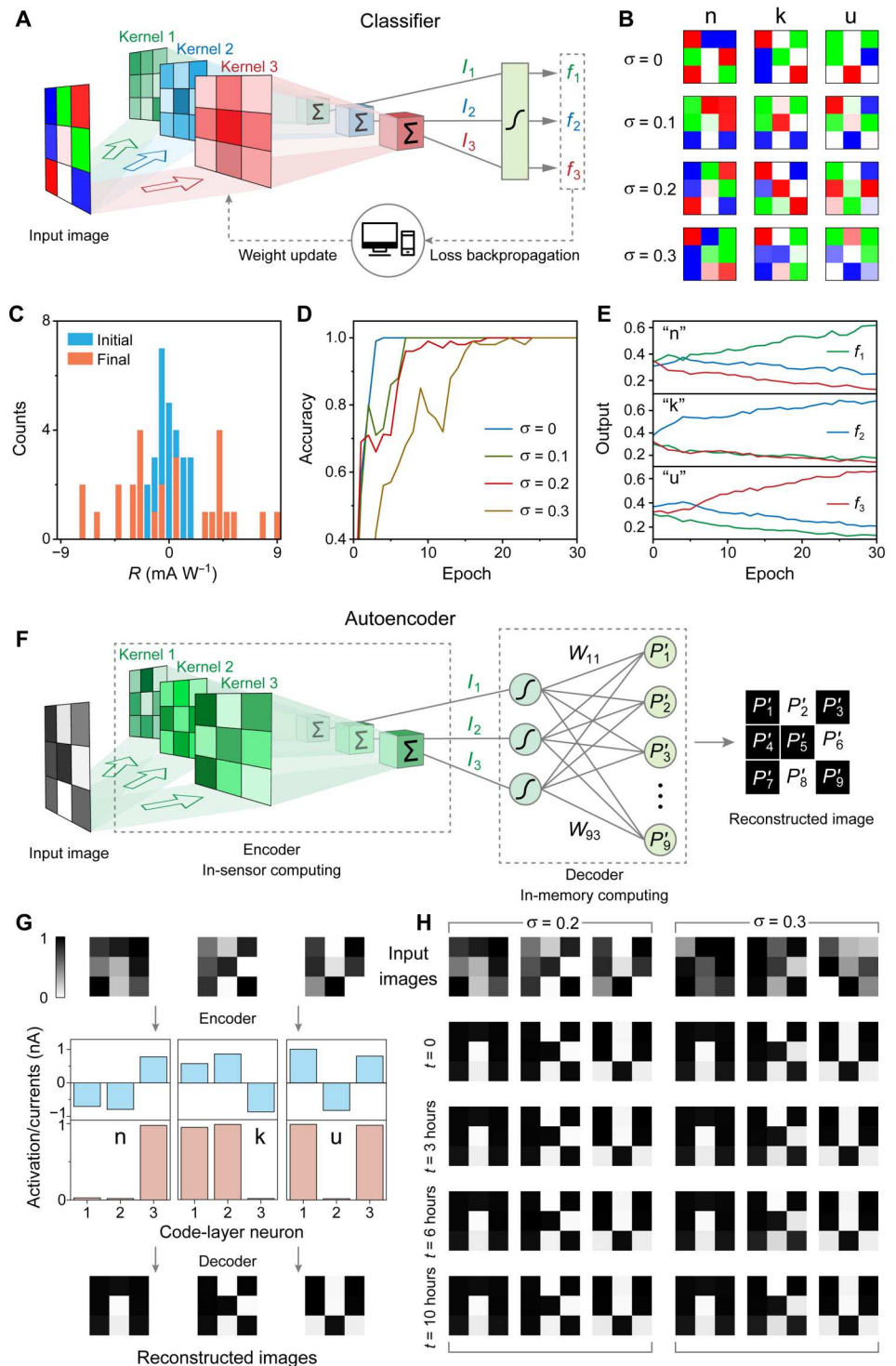
(σ = 0.2 and 0.3) were generated as the training and test datasets for the autoencoding task (fig. S40). The grayscale images were projected into the sensory kernels, and the total photocurrents of each kernel I_m were activated by the Sigmoid function, outputting a (3 × 1) encoded data. The encoded data were transformed to a vector of voltage signals and fed into the in-memory ANN for decoding. After the in-memory MAC operation, the currents measured from each output neurons I_n (n = 1, 2, ..., 9) were further nonlinearly activated (Sigmoid function), and the corresponding outputs P'_n were used to reconstructed a 3 × 3 pixel image. The network was trained, and backpropagation was performed to update the weights of the encoder and decoder (figs. S41 and S42); the loss evolution during the training is shown in fig. S43. Figure 5G presents the corresponding outputs of the

trained autoencoder for input images of n, k, and u. After in-sensor computing, each letter generates a unique encoded data close to binary, and the following in-memory computing can decode it into an image. The reconstructed images interpret the inputs correctly, with reduced noises and enhanced contrast. Figure 5H and fig. S44 depict the reconstructed images produced by the trained autoencoder with different times after the last training. The almost unchanged images undoubtedly demonstrate the local storage of the responsivities and conductance states in the networks, and, thus, the neuromorphic visual system can perform image sensing and processing tasks without external field.

DISCUSSION

Table S1 compares the parameters of the existing retinomorphic vision sensors with our device. The most important advantage of our device is that it can realize the nonvolatile modulation of the responsivity in a quite wide spectral range, which enables the implementation of in-sensor computing for broadband images. Of course, this device still suffers from some limitations for practical applications. (i) A drain bias is still required during the read process, inducing a high dark current and consuming more energy. (ii) The response speed is limited to milliseconds due to the charge trapping/detrapping mechanism, restricting its potential for high-speed image processing. (iii) Although it can operate in a wide spectral range, the discrimination of colors (wavelengths) is still a great challenge, and the wavelength-dependent photoresponse will affect the processing accuracy of the sensory network for color images. (iv) The scale of the sensory network is still limited, which is difficult in meeting the requirements of machine vision for millions of pixels and tens of categories in real scenarios. In the future, we will pay more efforts to solve these challenges. Fortunately, the photovoltaic effect provides a feasible approach to realize high-speed photoresponse in nanosecond timescale (1), and no drain bias is required for devices based on the photovoltaic effect. The RC delay, however, should also be fully considered for high-speed devices because the parasitic capacitance, together with the large resistance of the device, would induce a nonnegligible RC time constant, which limits the further improvement of the processing speed. Mimicking the various human cone cells (short-wave, middle-wave, and long-wave cones) that respond to specific wavelengths (38) might provide a possible approach to realize color discrimination. In addition, the compatibility of the device with modern complementary metal-oxide semiconductor (CMOS) technology is crucial for the large-scale fabrication of the sensory network. The polymer electrolyte used in this work is considered to be the main obstacle for CMOS process due to its poor thermodynamical stability and processability. Nevertheless, inorganic solid electrolyte (e.g., Li_3PO_4 and Li_xSiO_2) provides a promising candidate to replace the polymer electrolyte (39), which can improve the CMOS compatibility of our device. High-speed, low-power, and large-scale retinomorphic vision sensors with nonvolatile modulation of responsivity and color discrimination ability should be further developed in the future.

In conclusion, we have proposed a strategy that uses localized field induced by captured Li^+ ions instead of the externally controlled gate bias to realize nonvolatile modulation of responsivity. Moreover, correspondingly, retinomorphic vision sensors based on specially designed core-sheath SWNT@GDY have been developed to constitute built-in neural networks with locally stored weights, which can implement in-sensor convolutional processing in a wide spectral range covering 400 to 1800 nm. Closely analogous to human visual system, neuromorphic machine vision involving front-end in-sensor CNN and back-end in-memory ANN is constructed to implement supervised and unsupervised learning tasks. It is a great breakthrough for the development of in-sensor neural networks with locally stored responsivities, providing a feasible strategy to develop high-speed and low-power neuromorphic machine vision for real-time object recognition and classification.

MATERIALS AND METHODS
Device fabrication
Core-sheath SWNT@GDY nanotubes were synthesized via a solution-phase epitaxial strategy as described in note S1. The prepatterned source, drain, and side-gate electrodes (Cr/Au, 10/50 nm) of the device array were fabricated on an oxygen plasma–pretreated SiO_2/Si substrate (300-nm SiO_2) by photolithography, thermal evaporation, and liftoff processes. The SWNT@GDY channels with a thickness of approximately 10 nm were directly printed by an Aerosol Jet printer using core-sheath SWNT@GDY solution as inks, followed by an annealing process at 120°C for 30 min. An insulated polymethyl methacrylate (PMMA) layer was spin-coated on the device surface to protect the source and drain electrodes from contact with the electrolyte, and specific reaction windows on top of the channels and side gates were selectively exposed by electron-beam lithography. The ion-gel electrolyte was prepared by dissolving 30 mg of $LiClO_4$ (Sigma-Aldrich) and 100 mg of polyethylene oxide powders [weight-average molecular weight (M_w) = 100,000, Sigma-Aldrich] into 20 ml of anhydrous methanol. The mixture was stirred for 24 hours at 50°C. After that, the polymer electrolyte with a thickness of 1.2 μm was spin-coated on top of the PMMA layer, connecting the exposed SWNT@GDY channel and side-gate electrode (32). The electrolytes of each device were separated via selective etching to avoid interference between adjacent devices. Last, the device array was mounted and wire-bonded to a chip carrier for measurement.

Measurement setup
For electrical measurements, basic electrical characteristics were measured by a semiconductor analyzer (Keithley, 4200A-SCS). The gate pulses were applied by an arbitrary waveform generator (Tektronix, AFG31052). During the implementation of in-sensor and in-memory computing, drain voltages and corresponding output currents (photocurrents) were applied and measured using a set of source-measurement units (Keithley). For optical inputs, fiber lasers with tunable intensities and wavelengths of 405, 532, 633, 980, 1550, and 1800 nm were used. The 3 × 3 images generated by nine aligned lasers with corresponding wavelengths and intensities were projected onto the device array using a microscope (fig. S34).

Convolutional processing for hyperspectral images
Hyperspectral images with band numbers of 1, 60, and 130 were selected as images with spectra of UV, vis, and NIR, respectively. For simplicity, all these images were first compressed to 100 × 100 pixels. Each image was divided into a series of 3 × 3–pixel

subimages with a sliding step of 1 (fig. S29). The pixel values (0 to 255) of these subimages were converted to voltages that were used to control the intensity of input lasers with corresponding wavelengths (405 nm for UV, 633 nm for vis, and 1800 nm for NIR). These subimages were optically projected to a 3 × 3 sensor array in sequence, and the total photocurrents were measured by applying a drain voltage of 0.1 V. The responsivity distribution of the sensor array was set using a closed-loop programming method (fig. S20) one device by one device. The dark currents of the sensor array were measured before and after optical projection to calibrate the photocurrents. Through in-sensor MAC operations, each subimage was converted to a photocurrent value, and processed images were reconstructed by ranking the measured photocurrents in sequence.

Preparation of datasets

The training and test datasets used for classification and autoencoding were generated by Python. For classification task, we prepared four sets of training and test datasets with different Gaussian noises (σ = 0, 0.1, 0.2, and 0.3). For each training dataset, 200 images corresponding to letters of n, k, and u were randomly generated, and, then, colors (blue, green, and red) and noises (with corresponding σ) were randomly added to prepare color images. Test datasets containing 100 images were prepared in the same way. For autoencoding task, grayscale training and test datasets with different Gaussian noises (σ = 0.2 and 0.3) were prepared similarly, just remove the step of adding colors.

Implementation of image classification

The initial weights (responsivities) of the sensory network were randomly chosen with a Gaussian distribution. For each training epoch, a set of 20 color images was randomly chosen from the training dataset with corresponding noise level. These images were optically projected to three kernels (3 × 3), and the output photocurrents of each kernel I_m was given by

$$I_m = \sum_{i=1}^{3}\sum_{j=1}^{3} I_{m,ij} = \sum_{i=1}^{3}\sum_{j=1}^{3} P_{ij} \cdot R_{m,ij} \qquad (1)$$

where i and j represent the row and column indices, respectively. The above-described processes were executed on the sensor array hardware, and the following activation and backpropagation processes were performed on software. In detail, the measured I_m was activated by the Softmax function

$$f_m(I_m) = e^{I_m\xi} / \sum_{k=1}^{M} e^{I_k\xi} \qquad (2)$$

where $\xi = 10^9$ A^{-1} is the scaling factor for normalization, and $M = 3$ here corresponds to the number of classes. The output after activation f_m represents the predicted probability $\hat{y}_m$ corresponding to letters of n, k, and u, respectively, and the letter with the largest $\hat{y}_m$ is regarded as the classification result. There is only one convolutional layer and no pooling layer in this CNN network. After each epoch, the loss was calculated using the cross-entropy loss function

$$\mathcal{L} = -\sum_{k=1}^{M} y_k \log\hat{y}_k \qquad (3)$$

where y_k and $\hat{y}_k$ were the label and prediction, respectively. To update the weights of the neural network, the gradients of the loss function $\mathcal{L}$ was backpropagated

$$\Delta R_{m,ij} = \frac{\eta}{S}\sum_{k=1}^{S} \nabla_{R_{m,ij}}\mathcal{L}_k \qquad (4)$$

with learning rate η = 0.2 and the size of batch S = 20. The updated weights were programmed to the sensor array one device by one device, using the closed-loop programming method (note S3). The classification accuracies were measured by projecting 100 test images to the network in each epoch. The distributions of weights during and after training were measured one device by one device as shown in fig. S34E.

Implementation of autoencoding

The initial weights of the front-end CNN and back-end ANN networks were randomly chosen with a Gaussian distribution. The training of the autoencoder was performed by feeding 20 randomly chosen grayscale images to the CNN kernels for each epoch. The images were projected into the sensor array using 3 × 3 laser array (532 nm), and the responsivities in the three kernels were programmed to the corresponding values for 532-nm wavelength. The output photocurrents of each kernel I_m were measured and further nonlinearly activated using the Sigmoid function [$f_m(I_m) = (1 + e^{-I_m\xi})^{-1}$, where $\xi = 5 \times 10^9$ A^{-1}]. The encoded data were converted to sequential voltage pulses (6-bit precision) with six time intervals ($t_1, t_2, ..., t_6$) (7, 25), and the total output currents were summed by $I_n = \sum_{k=1}^{6}(I_k \times 2^{k-1})$ (fig. S45). The nine output currents I_n were also activated by the Sigmoid function (scaling factor $\xi = 3 \times 10^8$ A^{-1}). The mean square loss function $\mathcal{L} = \sum_{n=1}^{9}(P_n - P'_n)^2$ was used for backpropagation and weight update, where P_n and P'_n correspond to the intensity of the nth pixel in original and reconstructed images. The nonlinear activation and backpropagation processes in classification and autoencoding tasks were performed by software. After the last training, the weights (responsivity for encoder and conductance for decoder) and autoencoding tasks were measured every 1 hour.

Supplementary Materials

This PDF file includes:
Supplementary Notes 1 to 3
Figs. S1 to S45
Table S1
References

REFERENCES AND NOTES

1. L. Mennel, J. Symonowicz, S. Wachter, D. K. Polyushkin, A. J. Molina-Mendoza, T. Mueller, Ultrafast machine vision with 2D material neural network image sensors. *Nature* **579**, 62–66 (2020).

2. Y. Chai, In-sensor computing for machine vision. *Nature* **579**, 32–33 (2020).

3. D. Lee, M. Park, Y. Baek, B. Bae, J. Heo, K. Lee, In-sensor image memorization and encoding via optical neurons for bio-stimulus domain reduction toward visual cognitive processing. *Nat. Commun.* **13**, 5223 (2022).

4. F. Zhou, Y. Chai, Near-sensor and in-sensor computing. *Nat. Electron.* **3**, 664–671 (2020).

5. T. Wan, B. Shao, S. Ma, Y. Zhou, Q. Li, Y. Chai, In-sensor computing: Materials, devices, and integration technologies. *Adv. Mater.*, 2203830 (2022).

6. K. Liu, T. Zhang, B. Dang, L. Bao, L. Xu, C. Cheng, Z. Yang, R. Huang, Y. Yang, An optoelectronic synapse based on α-In$_2$Se$_3$ with controllable temporal dynamics for multimode and multiscale reservoir computing. *Nat. Electron.* **5**, 761–773 (2022).

7. Z. Zhang, X. Zhao, X. Zhang, X. Hou, X. Ma, S. Tang, Y. Zhang, G. Xu, Q. Liu, S. Long, In-sensor reservoir computing system for latent fingerprint recognition with deep ultraviolet photosynapses and memristor array. *Nat. Commun.* **13**, 6590 (2022).

8. L. Sun, Z. Wang, J. Jiang, Y. Kim, B. Joo, S. Zheng, S. Lee, W. J. Yu, B.-S. Kong, H. Yang, In-sensor reservoir computing for language learning via two-dimensional memristors. *Sci. Adv.* **7**, eabg1455 (2021).

9. F. Zhou, Z. Zhou, J. Chen, T. H. Choy, J. Wang, N. Zhang, Z. Lin, S. Yu, J. Kang, H. S. P. Wong, Y. Chai, Optoelectronic resistive random access memory for neuromorphic vision sensors. *Nat. Nanotechnol.* **14**, 776–782 (2019).

10. Y.-X. Hou, Y. Li, Z.-C. Zhang, J.-Q. Li, D.-H. Qi, X.-D. Chen, J.-J. Wang, B.-W. Yao, M.-X. Yu, T.-B. Lu, Large-scale and flexible optical synapses for neuromorphic computing and integrated visible information sensing memory processing. *ACS Nano* **15**, 1497–1508 (2021).

11. Z.-C. Zhang, Y. Li, J.-J. Wang, D.-H. Qi, B.-W. Yao, M.-X. Yu, X.-D. Chen, T.-B. Lu, Synthesis of wafer-scale graphdiyne/graphene heterostructure for scalable neuromorphic computing and artificial visual systems. *Nano Res.* **14**, 4591–4600 (2021).

12. B. Dang, K. Liu, X. Wu, Z. Yang, L. Xu, Y. Yang, R. Huang, One-phototransistor–one-memristor array with high-linearity light-tunable weight for optic neuromorphic computing. *Adv. Mater.*, 2204844 (2022).

13. C.-Y. Wang, S.-J. Liang, S. Wang, P. Wang, Z. Li, Z. Wang, A. Gao, C. Pan, C. Liu, J. Liu, H. Yang, X. Liu, W. Song, C. Wang, X. Wang, K. Chen, Z. Wang, K. Watanabe, T. Taniguchi, J. J. Yang, F. Miao, Gate-tunable van der Waals heterostructure for reconfigurable neural network vision sensor. *Sci. Adv.* **6**, eaba6173 (2020).

14. L. Pi, P. Wang, S.-J. Liang, P. Luo, H. Wang, D. Li, Z. Li, P. Chen, X. Zhou, F. Miao, T. Zhai, Broadband convolutional processing using band-alignment-tunable heterostructures. *Nat. Electron.* **5**, 248–254 (2022).

15. B. Cui, Z. Fan, W. Li, Y. Chen, S. Dong, Z. Tan, S. Cheng, B. Tian, R. Tao, G. Tian, D. Chen, Z. Hou, M. Qin, M. Zeng, X. Lu, G. Zhou, X. Gao, J.-M. Liu, Ferroelectric photosensor network: An advanced hardware solution to real-time machine vision. *Nat. Commun.* **13**, 1707 (2022).

16. X. Fu, T. Li, B. Cai, J. Miao, G. N. Panin, X. Ma, J. Wang, X. Jiang, Q. Li, Y. Dong, C. Hao, J. Sun, H. Xu, Q. Zhao, M. Xia, B. Song, F. Chen, X. Chen, W. Lu, W. Hu, Graphene/MoS$_{2-x}$O$_x$/graphene photomemristor with tunable non-volatile responsivities for neuromorphic vision processing. *Light-Sci. Appl.* **12**, 39 (2023).

17. S. Lee, R. Peng, C. Wu, M. Li, Programmable black phosphorus image sensor for broadband optoelectronic edge computing. *Nat. Commun.* **13**, 1485 (2022).

18. Y. Wang, Y. Cai, F. Wang, J. Yang, T. Yan, S. Li, Z. Wu, X. Zhan, K. Xu, J. He, Z. Wang, A three-dimensional neuromorphic photosensor array for nonvolatile in-sensor computing. *Nano Lett.* **23**, 4524–4532 (2023).

19. S. Wang, C.-Y. Wang, P. Wang, C. Wang, Z.-A. Li, C. Pan, Y. Dai, A. Gao, C. Liu, J. Liu, H. Yang, X. Liu, B. Cheng, K. Chen, Z. Wang, K. Watanabe, T. Taniguchi, S.-J. Liang, F. Miao, Networking retinomorphic sensor with memristive crossbar for brain-inspired visual perception. *Natl. Sci. Rev.* **8**, nwaa172 (2021).

20. X. Hong, Y. Huang, Q. Tian, S. Zhang, C. Liu, L. Wang, K. Zhang, J. Sun, L. Liao, X. Zou, Two-dimensional perovskite-gated AlGaN/GaN high-electron-mobility-transistor for neuromorphic vision sensor. *Adv. Sci.* **9**, 2202019 (2022).

21. F. Liao, Z. Zhou, B. J. Kim, J. Chen, J. Wang, T. Wan, Y. Zhou, A. T. Hoang, C. Wang, J. Kang, J.-H. Ahn, Y. Chai, Bioinspired in-sensor visual adaptation for accurate perception. *Nat. Electron.* **5**, 84–91 (2022).

22. T. Euler, S. Haverkamp, T. Schubert, T. Baden, Retinal bipolar cells: Elementary building blocks of vision. *Nat. Rev. Neurosci.* **15**, 507–519 (2014).

23. C. Li, M. Hu, Y. Li, H. Jiang, N. Ge, E. Montgomery, J. Zhang, W. Song, N. Dávila, C. E. Graves, Z. Li, J. P. Strachan, P. Lin, Z. Wang, M. Barnell, Q. Wu, R. S. Williams, J. J. Yang, Q. Xia, Analogue signal and image processing with large memristor crossbars. *Nat. Electron.* **1**, 52–59 (2018).

24. D. Ielmini, H.-S. P. Wong, In-memory computing with resistive switching devices. *Nat. Electron.* **1**, 333–343 (2018).

25. P. Yao, H. Wu, B. Gao, J. Tang, Q. Zhang, W. Zhang, J. J. Yang, H. Qian, Fully hardware-implemented memristor convolutional neural network. *Nature* **577**, 641–646 (2020).

26. A. Sebastian, M. Le Gallo, R. Khaddam-Aljameh, E. Eleftheriou, Memory devices and applications for in-memory computing. *Nat. Nanotechnol.* **15**, 529–544 (2020).

27. X.-H. Wang, Z.-C. Zhang, J.-J. Wang, X.-D. Chen, B.-W. Yao, Y.-X. Hou, M.-X. Yu, Y. Li, T.-B. Lu, Synthesis of wafer-scale monolayer pyrenyl graphdiyne on ultrathin hexagonal boron nitride for multibit optoelectronic memory. *ACS Appl. Mater. Interfaces* **12**, 33069–33075 (2020).

28. Z. C. Zhang, Y. Li, J. Li, X. D. Chen, B. W. Yao, M. X. Yu, T. B. Lu, J. Zhang, An ultrafast nonvolatile memory with low operation voltage for high-speed and low-power applications. *Adv. Funct. Mater.* **31**, 2102571 (2021).

29. F.-D. Wang, M.-X. Yu, X.-D. Chen, J. Li, Z.-C. Zhang, Y. Li, G.-X. Zhang, K. Shi, L. Shi, M. Zhang, T.-B. Lu, J. Zhang, Optically modulated dual-mode memristor arrays based on core-shell CsPbBr$_3$@graphdiyne nanocrystals for fully memristive neuromorphic computing hardware. *SmartMat* **4**, e1135 (2023).

30. X. Gao, Y. Zhu, D. Yi, J. Zhou, S. Zhang, C. Yin, F. Ding, S. Zhang, X. Yi, J. Wang, Ultrathin graphdiyne film on graphene through solution-phase van der Waals epitaxy. *Sci. Adv.* **4**, eaat6378 (2018).

31. Y. Li, Z. C. Zhang, J. Li, X.-D. Chen, Y. Kong, F.-D. Wang, G.-X. Zhang, T.-B. Lu, J. Zhang, Low-voltage ultrafast nonvolatile memory via direct charge injection through a threshold resistive-switching layer. *Nat. Commun.* **13**, 4591 (2022).

32. B. W. Yao, J. Li, X. D. Chen, M. X. Yu, Z. C. Zhang, Y. Li, T. B. Lu, J. Zhang, Non-volatile electrolyte-gated transistors based on graphdiyne/MoS$_2$ with robust stability for low-power neuromorphic computing and logic-in-memory. *Adv. Funct. Mater.* **31**, 2100069 (2021).

33. Z.-C. Zhang, X.-D. Chen, T.-B. Lu, Recent progress in neuromorphic and memory devices based on graphdiyne. *Sci. Technol. Adv. Mat.* **24**, 2196240 (2023).

34. E. J. Fuller, S. T. Keene, A. Melianas, Z. Wang, S. Agarwal, Y. Li, Y. Tuchman, C. D. James, M. J. Marinella, J. J. Yang, A. Salleo, A. A. Talin, Parallel programming of an ionic floating-gate memory array for scalable neuromorphic computing. *Science* **364**, 570–574 (2019).

35. Y. van de Burgt, E. Lubberman, E. J. Fuller, S. T. Keene, G. C. Faria, S. Agarwal, M. J. Marinella, A. Alec Talin, A. Salleo, A non-volatile organic electrochemical device as a low-voltage artificial synapse for neuromorphic computing. *Nat. Mater.* **16**, 414–418 (2017).

36. J. Wen, W. Tang, Z. Kang, Q. Liao, M. Hong, J. Du, X. Zhang, H. Yu, H. Si, Z. Zhang, Y. Zhang, Direct charge trapping multilevel memory with graphdiyne/MoS$_2$ van der waals heterostructure. *Adv. Sci.* **8**, 2101417 (2021).

37. J. Li, Z. Zhang, Y. Kong, B. Yao, C. Yin, L. Tong, X. Chen, T. Lu, J. Zhang, Synthesis of wafer-scale ultrathin graphdiyne for flexible optoelectronic memory with over 256 storage levels. *Chem* **7**, 1284–1296 (2021).

38. B. R. Conway, Color vision, cones, and color-coding in the cortex. *Neuroscientist* **15**, 274–290 (2009).

39. Y. Li, J. Lu, D. Shang, Q. Liu, S. Wu, Z. Wu, X. Zhang, J. Yang, Z. Wang, H. Lv, M. Liu, Oxide-based electrolyte-gated transistors for spatiotemporal information processing. *Adv. Mater.* **32**, 2003018 (2020).

40. M. Gomroki, M. Hasanlou, P. Reinartz, STCD-EffV2T Unet: Semi transfer learning Efficient-NetV2 T-Unet network for urban/land cover change detection using Sentinel-2 satellite images. *Remote Sens. (Basel)* **15**, 1232 (2023).

41. G. Li, Y. Li, H. Liu, Y. Guo, Y. Li, D. Zhu, Architecture of graphdiyne nanoscale films. *Chem. Commun.* **46**, 3256–3258 (2010).

42. J. Yao, Y. Li, Y. Li, Q. Sui, H. Wen, L. Cao, P. Cao, L. Kang, J. Tang, H. Jin, S. Qiu, Q. Li, Rapid annealing and cooling induced surface cleaning of semiconducting carbon nanotubes for high-performance thin-film transistors. *Carbon* **184**, 764–771 (2021).

43. Y. Liu, F. Wang, X. Wang, X. Wang, E. Flahaut, X. Liu, Y. Li, X. Wang, Y. Xu, Y. Shi, R. Zhang, Planar carbon nanotube-graphene hybrid films for high-performance broadband photodetectors. *Nat. Commun.* **6**, 8589 (2015).

44. S. Dai, Y. Zhao, Y. Wang, J. Zhang, L. Fang, S. Jin, Y. Shao, J. Huang, Recent advances in transistor-based artificial synapses. *Adv. Funct. Mater.* **29**, 1903700 (2019).

45. S. Jiang, S. Nie, Y. He, R. Liu, C. Chen, Q. Wan, Emerging synaptic devices: From two-terminal memristors to multiterminal neuromorphic transistors. *Mater. Today Nano* **8**, 100059 (2019).

46. J. Jiang, J. Guo, X. Wan, Y. Yang, H. Xie, D. Niu, J. Yang, J. He, Y. Gao, Q. Wan, 2D MoS$_2$ neuromorphic devices for brain-like computational systems. *Small* **13**, 1700933 (2017).

47. D. Liu, Q. Shi, S. Dai, J. Huang, The design of 3D-interface architecture in an ultralow-power, electrospun single-fiber synaptic transistor for neuromorphic computing. *Small* **16**, 1907472 (2020).

48. C. S. Yang, D. S. Shang, N. Liu, E. J. Fuller, S. Agrawal, A. A. Talin, Y. Q. Li, B. G. Shen, Y. Sun, All-solid-state synaptic transistor with ultralow conductance for neuromorphic computing. *Adv. Funct. Mater.* **28**, 1804170 (2018).

49. E. J. Fuller, F. E. Gabaly, F. Léonard, S. Agarwal, S. J. Plimpton, R. B. Jacobs-Gedrim, C. D. James, M. J. Marinella, A. A. Talin, Li-ion synaptic transistor for low power analog computing. *Adv. Mater.* **29**, 1604310 (2017).

50. J. Lee, L. G. Kaake, J. H. Cho, X. Y. Zhu, T. P. Lodge, C. D. Frisbie, Ion gel-gated polymer thin-film transistors: Operating mechanism and characterization of gate dielectric capacitance, switching speed, and stability. *J. Phys. Chem. C* **113**, 8972–8981 (2009).

51. C. Sun, D. J. Searles, Lithium storage on graphdiyne predicted by DFT calculations. *J. Phys. Chem. C* **116**, 26222–26226 (2012).

52. N. Wang, J. He, K. Wang, Y. Zhao, T. Jiu, C. Huang, Y. Li, Graphdiyne-based materials: Preparation and application for electrochemical energy storage. *Adv. Mater.* **31**, 1803202 (2019).

53. K. Kim, C.-L. Chen, T. Quyen, A. M. Shen, Y. Chen, A carbon nanotube synapse with dynamic logic and learning. *Adv. Mater.* **25**, 1693–1698 (2013).

54. S. Kazaoui, N. Minami, H. Kataura, Y. Achiba, Absorption spectroscopy of single-wall carbon nanotubes: Effects of chemical and electrochemical doping. *Synth. Met.* **121**, 1201–1202 (2001).

ScienceAdvances

Broadband sensory networks with locally stored responsivities for neuromorphic machine vision

Guo-Xin Zhang, Zhi-Cheng Zhang, Xu-Dong Chen, Lixing Kang, Yuan Li, Fu-Dong Wang, Lei Shi, Ke Shi, Zhi-Bo Liu, Jian-Guo Tian, Tong-Bu Lu, and Jin Zhang

View the article online
https://www.science.org/doi/10.1126/sciadv.adi5104
Permissions
https://www.science.org/help/reprints-and-permissions

Use of this article is subject to the Terms of service